1

Refining Planetary Boundary Layer Height Retrievals from Micropulse-lidar at Multiple ARM Sites Around the World

Natalia Roldán-Henao[1], Tianning Su[1], Zhanqing Li[1]

[1]Department of Atmospheric and Oceanic Sciences and ESSIC, University of Maryland, College Park, Maryland 20740, USA

Corresponding author: Zhanqing Li (zhanqing@umd.edu) and Tianning Su (tianning@umd.edu)

Key Points:

- This study evaluates the performance of the new DTDS algorithm at 5 Department of Energy's Atmospheric Radiation Measurement sites.
- DTDS-derived boundary layer dataset outperforms existing lidar-derived products at all five sites, offering a more precise representation.
- This study provides an extensive boundary layer height dataset that paves the way for future investigations in various applications.

Abstract

15

16 Knowledge of the Planetary Boundary Layer Height (PBLH) is crucial for various applications
17 in atmospheric and environmental sciences. Lidar measurements are frequently used to monitor
18 the evolution of the PBLH, providing more frequent observations than traditional radiosonde-
19 based methods. However, lidar-derived PBLH estimates have substantial uncertainties,
20 contingent upon the retrieval algorithm used. In addressing this, we applied the Different
21 Thermo-Dynamic Stabilities (DTDS) algorithm to establish a PBLH dataset at five separate
22 Department of Energy's Atmospheric Radiation Measurement (ARM) sites across the globe.
23 Both the PBLH methodology and the products are subject to rigorous assessments in terms of
24 their uncertainties and constraints, juxtaposing them with other products. The DTDS-derived
25 product consistently aligns with radiosonde PBLH estimates, with correlation coefficients
26 exceeding 0.77 across all sites. This study delves into a detailed examination of the strengths and
27 limitations of PBLH datasets with respect to both radiosonde-derived and other lidar-based
28 estimates of the PBLH by exploring their respective errors and uncertainties. It is found that
29 varying techniques and definitions can lead to diverse PBLH retrievals due to the inherent
30 intricacy and variability of the boundary layer. Our DTDS-derived PBLH dataset outperforms
31 existing products derived from ceilometer data, offering a more precise representation of the
32 PBLH. This extensive dataset paves the way for advanced studies and an improved
33 understanding of boundary-layer dynamics, with valuable applications in weather forecasting,
34 climate modelling, and environmental studies.

Plain Language Abstract

35

36 The Planetary Boundary Layer (PBL) is the lowest region of the atmosphere directly influenced
37 by Earth's surface. This layer is vital as it connects the atmosphere to surface processes. Given its
38 importance, accurately determining its height (PBLH) is crucial for weather, climate, and air
39 quality studies. However, current PBLH estimates either have infrequent time intervals, as seen
40 with radiosondes, or face notable uncertainties, like those derived from remote sensing
41 techniques. This research evaluates a new lidar-based PBLH method at five Department of
42 Energy's Atmospheric Radiation Measurement sites across the globe. The PBLH dataset from the
43 new methodology aligns well with radiosonde, with notably smaller biases compared to the
44 existing products. Additionally, this study investigates potential errors in our PBLH data,
45 revealing that varying techniques and definitions can produce different PBLH values,
46 highlighting the complex and dynamic nature of the PBL.

1 Introduction

47

48 The Planetary Boundary Layer (PBL) is the lowest section of the troposphere, significantly
49 influenced by terrestrial surfaces. This layer reacts to surface forcings, such as frictional drag and
50 heat transfer, and is instrumental in regulating pollutant emission and dissipation. Interactions
51 between the atmosphere and the surface culminate in substantial variations in the PBL Height
52 (PBLH) across both spatial and temporal dimensions. Temporal fluctuations can emerge within
53 an hour, while spatial changes may span several hundred meters to a few kilometers (Stull,
54 1988). The PBL exerts a pivotal influence on numerous atmospheric processes and applications,
55 ranging from the dispersion of air pollutants to weather forecasting and climate modeling (Guo et
56 al., 2016; Hu et al., 2010; Knote et al., 2015; Li et al., 2017; Seidel et al., 2010; Su et al., 2023).

57 Hence, the precise estimation of PBLH is vital to advancing our understanding of surface-
58 atmospheric processes and refining climate and weather simulations. Yet, the measurement and
59 modeling of PBLH pose significant challenges due to its high variability and limitations inherent
60 in observational technology.

61 Traditionally, the estimation of PBLH has relied on in-situ radiosonde (RS) data, capturing
62 thermodynamic profiles of temperature, humidity, and wind across various pressure levels (Li et
63 al., 2021; Seidel et al., 2010; W. Zhang et al., 2018). Methods used in conjunction with RS data
64 include surface-based inversions, relative humidity, and potential temperature gradient methods,
65 Richardson number methods, and the parcel method (Bradley et al., 1993; Liu & Liang, 2010;
66 Seidel et al., 2010; Vogelezang & Holtslag, 1996), among others.

67 While RSs have been employed as a standard in estimating PBLH, their precision varies notably
68 depending on atmospheric thermodynamic conditions, with no single method proving universally
69 effective across all conditions (Li et al., 2021). Furthermore, RS retrievals face restrictions in
70 terms of spatial coverage and observational frequency, typically occurring only twice daily at
71 most stations. In recent decades, lidar techniques have emerged as a potent alternative for PBLH
72 estimation, offering a very high frequency, albeit with a lesser degree of accuracy compared to
73 RS techniques (Eresmaa et al., 2006; Liu et al., 2018; Sawyer & Li, 2013; D. Zhang et al., 2022).
74 Lidar beams trace the diurnal evolution of the PBLH, measuring the backscattered radiation from
75 aerosols confined within the PBL. Ideally, aerosols within the PBL create a pronounced contrast
76 with the free atmosphere, facilitating the estimation of PBLH. However, lidars may struggle to
77 estimate PBLH under clean or highly stratified atmospheric conditions.

78 While the Different Thermo-Dynamic Stabilities (DTDS) method (Su et al., 2020) has
79 showcased reasonably good accuracy in PBLH estimation at the Southern Great Plains (SGP)
80 site, it is crucial to authenticate its performance in other regions. Moreover, the generation of a
81 more precise PBLH dataset for these areas can deepen our understanding of the PBL's behaviour
82 across diverse geographical regions with distinct climate regimes. As a result, this study aims to
83 examine the DTDS algorithm's efficacy in estimating PBLH at five distinct Department of
84 Energy (DOE) Atmospheric Radiation Measurement (ARM) sites. These comprise the SGP site
85 and four ARM Mobile Facilities, namely the Green Ocean Amazon – GoAmazon (MAO); the
86 Cloud, Aerosol, and Complex Terrain Interactions – CACTI (COR); the Convective and
87 Orographically-Induced Precipitation Study (FKB), and the Biogenic Aerosols – Effects on
88 Clouds and Climate – BAECC (TMP).

89 This paper is organized as follows. Section 2 briefly elucidates the ground-based measurements
90 at the ARM sites and the methodologies employed for calculating the PBLH. Section 3 presents
91 the results, further subdivided into an overview of the PBLH product retrieved using the DTDS
92 algorithm (hereinafter referred to as DTDS-PBLH), an assessment of DTDS-PBLH's
93 performance against RS PBLH (RS-PBLH), comparison with another lidar-based PBL product
94 using ceilometer data and investigate their errors and limitations. The final section provides a
95 concise discussion and concludes the paper.

96 **2 Data and Methodology**

97 The PBLH varies significantly from site to site according to multiple climatic and meteorological
98 conditions, both of which are highly determined by the geographical location of each site. To
99 comprehensively evaluate the performance of the DTDS algorithm, the present study estimates
100 the PBLH over five different DOE ARM sites, including one permanent location and four mobile
101 facilities. ARM ground observation facilities have provided continuous and comprehensive
102 measurements of all meteorological variables in the atmosphere and at the surface since the early
103 1990s. Specifically, this study draws information from the SGP site in the United States, the
104 MAO site of the GoAmazon campaign in Brazil, the COR site of the CACTI campaign in
105 Argentina, the FKB site of the COPS campaign in Germany, and the TMP site of the BAECC
106 campaign in Finland. These sites were selected to address different scientific objectives, but their
107 observational configurations are more or less standard, including the characterization of
108 boundary-layer meteorology. Regarding surface characteristics, we only consider continental
109 sites not influenced by a marine environment because the original DTDS algorithm was
110 developed using data collected at the SGP site. Also, only those sites with more than six months
111 of data are considered. Figure 1 shows the geographical distribution of the five sites selected.
112 Table 1 summarizes each site's specifications, including their latitude, longitude, altitude, period
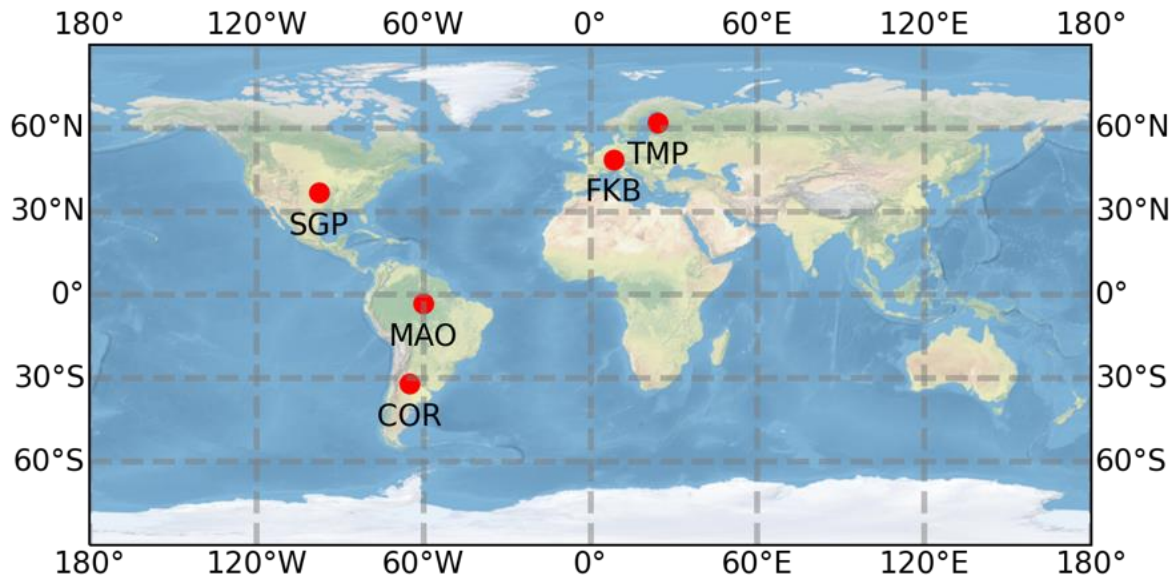113 of observations, and the cloud product used in this study.

114

115 **Figure 1.** Geographical distribution of the five DOE ARM sites used in this investigation.

116

117 **Table 1.** ARM site specifics and periods of observation used in this investigation.

ARM site	Latitude	Longitude	Elevation (m.a.s.l.)	Period of observations	Cloud Product
SGP	36° 36′ 26.3592″ N	97° 29′ 15.5148″ W	315	April 2001 – November 2019	CLDTYPE
MAO	3° 12′ 46.692″ S	60° 35′ 53.16″ W	50	January 2014 – November 2015	CEIL
COR	32° 4′ 0.912″ S	64° 52′ 53.58″	1141	October 2018 –	KAZRARSCL

		W		April 2019	
TMP	61° 50′ 34.8″ N	24° 17′ 16.8″ E	179	February 2014 – September 2014	KAZRARSCL
FKB	48° 32′ 24.36″ N	8° 23′ 48.48″ E	511	April 2007 – December 2007	KAZRARSCL

118 m.a.s.l.: meters above sea level

2.1 Estimation of the PBLH using RS measurements

120 The ARM SONDE product includes atmospheric thermodynamic profiles obtained from its
121 balloon-borne sounding system. These profiles contain height/pressure, temperature, humidity,
122 wind speed and direction data, captured at least four times daily (at 05:30, 11:30, 17:30, and
123 23:30 UTC) at each of the five ARM sites selected. Holdridge (2020) provide details about the
124 SONDE product. This study used only RS data collected between 06:30 and 19:00 Local Time
125 (LT). Because the vertical resolution of RS measurements fluctuates in accordance with the
126 balloon's ascent rate, we resampled RS data through linear interpolation to attain a vertical
127 resolution of five hPa.

128 We calculated the PBLH from radiosonde observations (i.e., RS-PBLH) using the well-
129 established Liu and Liang (2010) method. The method starts by distinguishing the
130 thermodynamics of the PBL according to the near-surface potential temperature difference.
131 Under convective conditions, this method identifies the PBLH as the height at which an air
132 parcel rising adiabatically becomes neutrally buoyant. The method first scans upward a level k,
133 where the temperature difference $\theta_k - \theta_1$ exceeds a threshold value. This level is corrected by a
134 second scan searching for the overshooting level, which defines the entrainment zone. Under
135 stable conditions, the PBLH is harder to determine because turbulence arises from buoyancy or
136 wind shear. Liu and Liang's method defines a stable PBLH as either the top of the stable layer
137 above the ground or at the low-level-jet nose height, whichever is lower.

2.2 Estimation of the PBLH using micropulse lidar measurements and the DTDS algorithm

139 Operating at 532 nm in both parallel and perpendicular polarizations, the autonomous, ground-
140 based Micropulse Lidar (MPL) provides backscattered radiation profiles at a temporal resolution
141 of 10–30 seconds and a vertical resolution of 30 m. Raw data are corrected for background
142 subtraction, signal saturation, overlap, after-pulse, and range per standard lidar-data processes
143 (Campbell et al., 2002, 2003). Quality-control flags help to omit erroneous data.

144 In principle, an inversion layer caps the PBLH, trapping moisture and aerosols within the
145 boundary layer, thus creating a sharp contrast with the free atmosphere (Seibert, 2000). This
146 contrast, visible in the backscattered radiation observed by lidar instruments, makes them ideal
147 for estimating the PBLH. However, estimating the PBLH from lidar data is challenging when
148 there is strong atmospheric stratification or when the inversion layer resides beneath the lidar
149 blind zone. These situations occur more frequently during stable boundary-layer conditions (Li et
150 al., 2017). Compared to the previous approaches. DTDS methods have made several
151 refinements. First, DTDS incorporates both the wavelength and gradient methods. In addition,
152 DTDS considers the diurnal variations of the boundary layer, allowing for a more comprehensive
153 estimation of the PBLH with enhanced vertical consistency and temporal continuity,

154 distinguishing it from the traditional method that relies solely on a single backscatter profile and
155 does not consider the diurnal cycle.

156 Traditional methods face challenges when estimating the PBLH under cloudy conditions, leading
157 to potential cloud contamination. To address this issue, the DTDS approach effectively handles
158 cloudy conditions by assessing the cloud-surface coupling. DTDS uses Lidar-derived PBLH,
159 cloud position, and the lifted condensation level to classify clouds as coupled or decoupled to the
160 surface. This differentiation of clouds aids in accurately diagnosing the PBLH (Su et al., 2022).
161 All these refinements in DTDS offer more reliable and robust PBLH estimations, even in
162 complex atmospheric conditions.

163 In this study, minor modifications were made to adapt the method to various scenarios. Firstly,
164 we tailored the time zone configurations for each site to ensure that DTDS correctly represents
165 the growing and decaying period of the boundary layer according to the geographical location.
166 Secondly, SGP blind zone is ~0.2 km, which makes DTDS retrieve the PBLH above this level.
167 We adjusted the blind zone of MAO, TMP, and COR to ensure peak efficiency. Thirdly, instead
168 of using the traditional morning radiosonde measurements, we opted to use the lifted
169 condensation level (LCL) as the upper boundary for determining the initial position of PBLH to
170 avoid the interference of the morning residual layer. The LCL was estimated from surface
171 meteorological data (relative humidity, temperature, pressure) based on an exact expression
172 (Romps, 2017). Therefore, our primary use of the radiosonde data was for validation purposes
173 only. Finally, we expanded the dataset's span, incorporating over 20 years of data, marking a
174 significant augmentation from the earlier evaluation duration of 8 years, as reported by Su et al.
175 (2020).

2.3 ARM PBLH product based on ceilometer measurements

177 ARM provides continuous estimates of the PBLH using ceilometers (i.e., Ceil-PBLH) at four of
178 the five ARM observatories used in this study: SGP, MAO, COR, and TMP. Specifically, ARM
179 deploys Vaisala CL31 ceilometers, which have a maximum vertical range of 7.7 km (Münkel
180 and Räsänen, 2004). The Vaisala CL31 ceilometer provides a total attenuated backscatter
181 coefficient profile at 910 nm, with a vertical resolution of 10 m and a temporal resolution of 2 s
182 (Münkel et al., 2007). The ARM Ceil-PBLH method starts by averaging the backscatter data to a
183 temporal resolution of 16 s, after which the well-known gradient method is applied. This method
184 searches for local gradient minima of the corrected total backscatter signal. Additionally, the
185 ARM Ceil-PBLH product excludes cloud and precipitation cases and suppresses false layer
186 identification (D. Zhang et al., 2022). In this study, we compared the performance of the DTDS
187 algorithm against this existing ARM-PBLH product.

3 Results and Discussion

3.1 Overview of the DTDS-derived PBLH product

190 Figure 2 shows typical examples of normalized backscatter signals measured by MPLs at the five
191 ARM observatories. Also shown are DTDS-derived PBLHs, radiosonde estimates derived
192 following Liu and Liang (2010), and ceilometer-derived PBLHs (based on the gradient method).
193 Figure 2a shows the evolution of the PBL at the SGP in wintertime as an example. During this

194 season, it is common to have little diurnal variation in the boundary layer, so the aerosol
195 structure tends to be highly stratified. This stratification usually complicates the retrieval of the
196 PBLH based on lidar techniques, with most retrieval algorithms performing poorly. In this SGP
197 case, the DTDS algorithm correctly captures the boundary layer's evolution and matches the RS-
198 PBLH estimates, even in the presence of a stratified aerosol layer. Contrary to the DTDS-PBLH
199 retrievals, Ceil-PBLH retrievals have multiple gaps and large jumps between different
200 atmospheric layers, not representing the PBLH well.

201
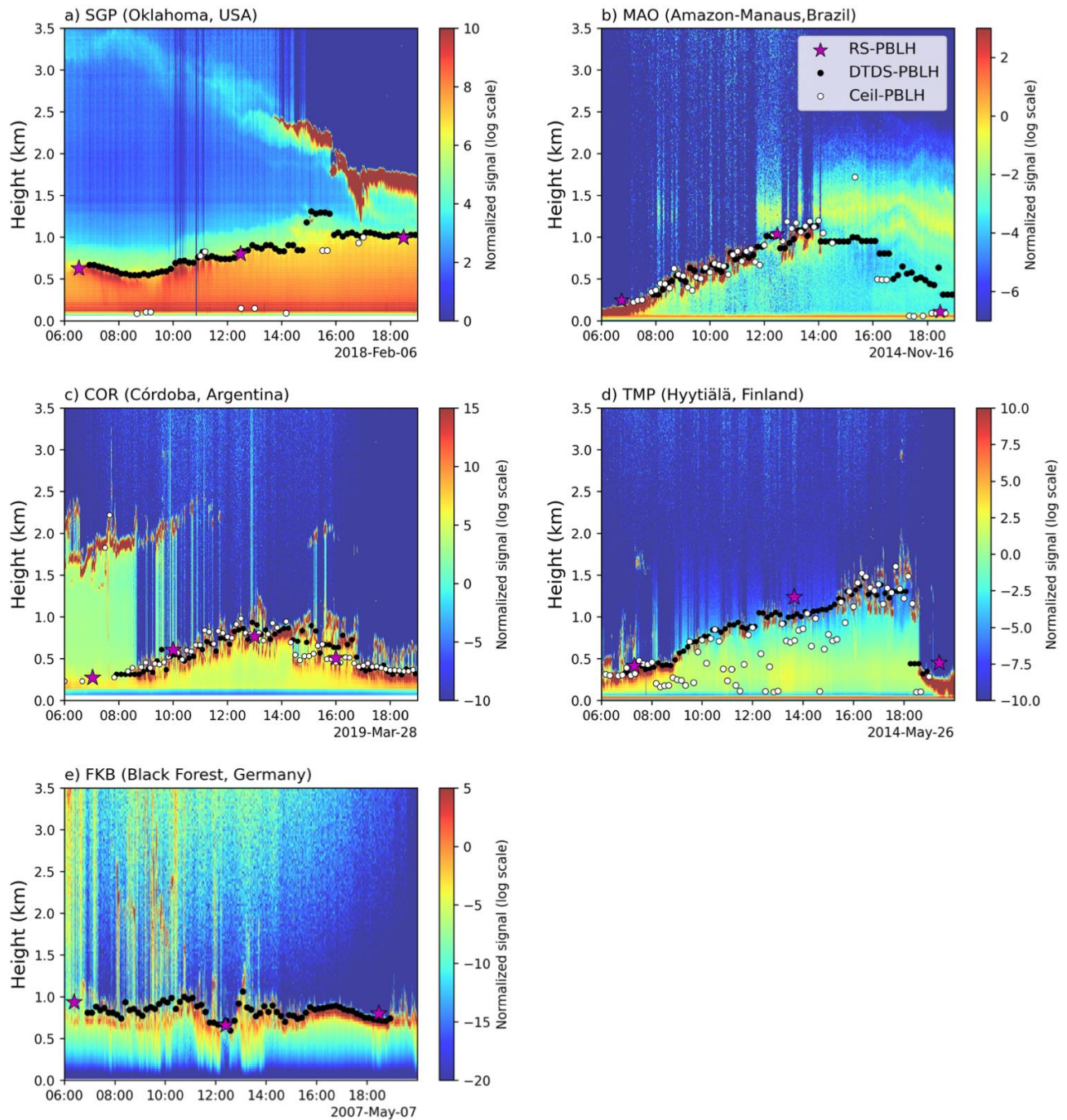
Figure 2. Examples of the computed PBLH at the five ARM sites using the DTDS algorithm (black dots), the ARM ceilometer product (white dots), and radiosonde estimates (magenta stars). The colormap corresponds to the normalized backscatter signal measured by the MPL at each site.

206   The MAO example shown in Fig. 2b shows a nocturnal boundary layer initially capped with
207   boundary-layer clouds. Clouds induce a strong step signal in the lidar backscatter and depending
208   on the type of cloud, can either facilitate or interfere with the PBLH retrieval. In the MAO
209   example, these boundary-layer clouds help define the PBLH. The DTDS-PBLH and Ceil-PBLH
210   retrievals agree well and are consistent with the RS-PBLH estimates. Around 14 LT, the cloud
211   signal disappears in the backscatter profile, exposing a more complex aerosol structure with
212   multiple aerosol layers and complicating the PBLH retrieval. The DTDS retrievals consistently
213   track the PBLH, while the Ceil-PBLH retrievals jump between different atmospheric layers,
214   showing some gaps. Similar to MAO during the morning hours, the COR example in Fig. 2c
215   represents a situation where the PBL is capped with boundary-layer clouds that accurately define
216   the PBLH. Both the DTDS-PBLH and Ceil-PBLH retrievals are similar throughout the day.

217   Figure 2d shows an example for TMP. In this case, the PBL is also capped with boundary-layer
218   clouds. However, the Ceil-PBLH retrievals considerably fluctuate between different atmospheric
219   levels. One explanation for such a poor performance might be that the ceilometer algorithm
220   computes the PBLH at each time step without considering the previous estimate, likely causing a
221   significant variation of the retrieval at every time point. Note that the DTDS-PBLH algorithm
222   consistently tracks the development of the PBLH without any significant fluctuations in the
223   retrieval.

224   Unlike the other sites analyzed, the MPL deployed at the FKB site was not fully calibrated,
225   having neglected the afterpulse correction (Fig. 2e). This complicates PBLH retrievals from that
226   site, more prominently noticeable under clear-sky conditions. In the example shown, the PBL
227   capped with boundary-layer clouds stays at a relatively constant height (~1 km) throughout the
228   day. Even without the afterpulse correction, DTDS-PBLH and RS-PBLH retrievals match well.

229   In addition to examining cases on specific days, it is also insightful to investigate the climatology
230   of the diurnal cycle when assessing the performance of the DTDS algorithm at the five different
231   sites. Figure 3 shows box-and-whisker plots for the diurnal cycles of the DTDS-PBLH retrievals
232   at the five ARM sites. In general, the PBLH is a shallow layer during the morning hours between
233   06:00 to 09:00 am (6–9 LT). The lowest morning layer is found at FKB, where the entire
234   distribution between 6:00 am and 7:00 am (6–7 LT) is below 500 meters above ground level
235   (m.a.g.l). COR has a maximum PBLH in the morning hours, with layers extending as high as 1.5
236   km a.g.l. Between 8:00 am and 10:00 am (8–10 LT), the PBLH grows as the turbulent eddies
237   progressively become larger, responding to a warmer surface. Looking at the mean values
238   (orange lines), this increment is steeper for MAO, a tropical region near the equator with a
239   continuous energy surplus. FKB also has a steep increment after 8:00 am. One of the reasons
240   could be that FKB's measurements were made in the summertime to understand the intense
241   orographic convection in this region. The PBLH reaches a maximum in the afternoon, occurring
242   at different times depending on the site. For instance, the PBLH at the SGP site reaches its
243   maximum around 4:00 pm, while places like MAO and COR have their maximum between noon
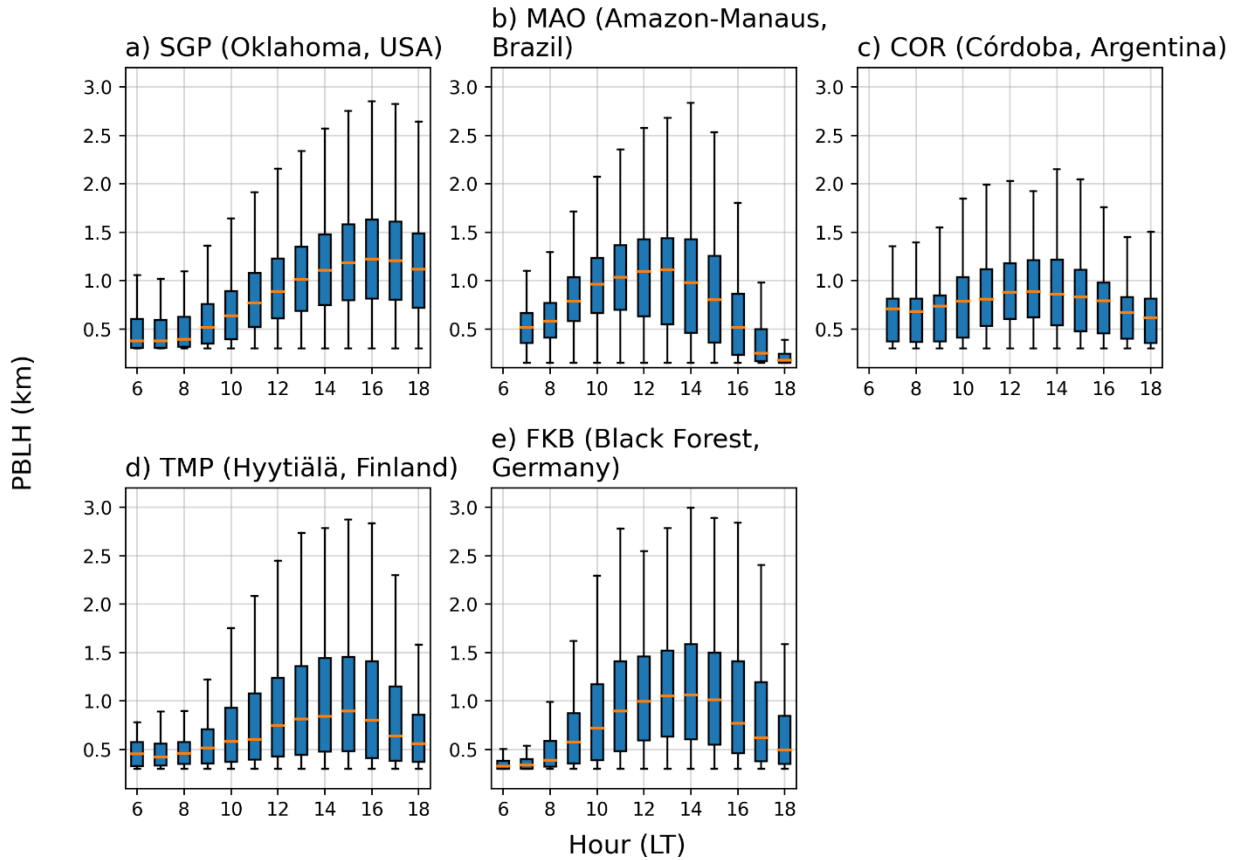244   and 1:00 pm. The PBLH decays in the late afternoon.

Figure 3. Climatologies of the diurnal cycle of PBLH computed using the DTDS algorithm at the five ARM observatories. The horizontal orange lines, blue bars, and whiskers represent median values, interquartile ranges, and ranges of the data, respectively. Time along the x-axis is Local Time (LT).

3.2 Evaluation of the DTDS-PBLH product

Figure 4 compares PBLH estimates obtained by the ceilometer method and derived from radiosondes at four of the five ARM sites. Note that FKB is not included in this figure because the Ceil-PBLH product is not available. Kernel density estimates (KDEs), which is a non-parametric technique that provides a continuous estimate of the probability density function of a dataset, in this case, the PBLH, are shown. Also given are the correlation coefficients (Rs), the Root-Mean-Square Errors (RMSEs), and the Mean Absolute Errors (MAEs) between the DTDS-PBLH and the RS-PBLH retrievals. In general, the relation between Ceil-PBLH and RS-PBLH is highly dispersed, with R ranging from 0.49 at TMP to 0.63 at MAO, RMSE oscillating between 0.55 and 0.74 km, and MAE between 0.33 and 0.49km.
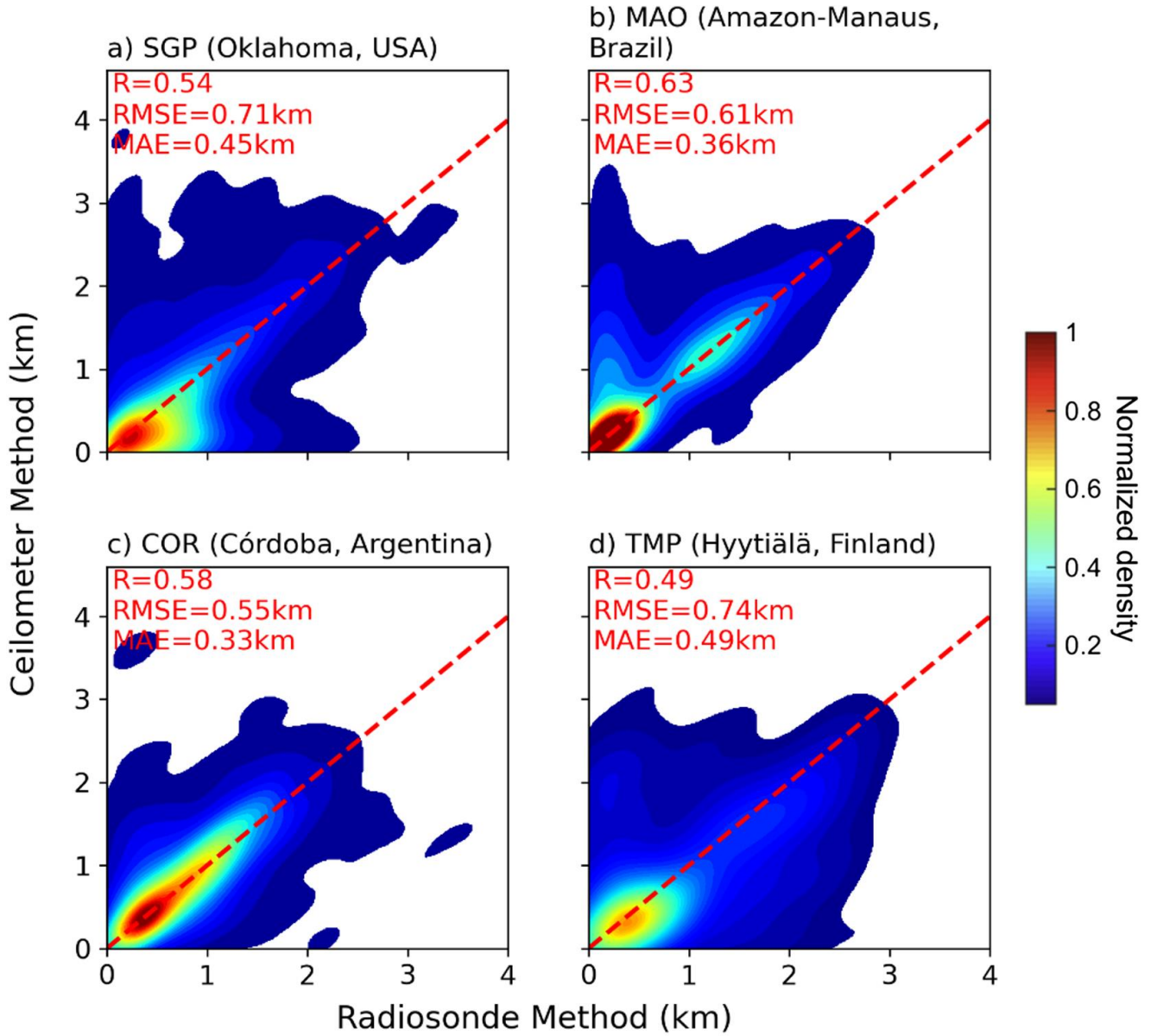
261
262 **Figure 4.** Kernel distribution estimates of ARM ceilometer- and radiosonde-derived PBLHs at
263 the five ARM sites. The correlation coefficient (R), root-mean-square error (RMSE), and mean
264 absolute error (MAE) are given in each panel. Dashed red lines correspond to 1:1 lines.

265   Figure 5 illustrates the same analysis as Fig. 4, but instead of using the Ceil-PBLH dataset,
266   DTDS-PBLH and RS-PBLH retrievals are compared. The DTDS-PBLH algorithm outperforms
267   the Ceil-PBLH method at every site, with higher correlations and smaller errors. Figure 4 also
268   shows a strong linear relationship between both sets of retrievals, with R values ranging from
269   0.77 at COR to 0.93 at MAO. These higher correlations, in comparison with the ceilometer
270   method, attest to the effectiveness of the DTDS algorithm in resolving the temporal evolution of
271   the PBLH. The robustness of the DTDS algorithm is also echoed in the error values. Specifically,
272   RMSEs oscillate between 0.27 and 0.41 km, approximately 0.3 km smaller than the RMSE found
273   with Ceil-PBLH, and MAEs oscillate between 0.18 to 0.27 km. approximately 0.2 km smaller
274   than Ceil-PBLH. Figure 6 summarizes the information from Figs. 3 and 4.

275   Figure 5 shows that the DTDS algorithm tends to overestimate shallow boundary layers,
276   typically below 1 km, and underestimate deep boundary layers. Such a situation is particularly
277   noticeable at the SGP sites. At the MAO site, the overestimation of the PBLH is more noticeable.
278   In particular, MAO is located in a tropical region where the PBL expands to significant altitudes
279   during the afternoon, fueled by the surplus of energy prevalent in these regions. However, the
280   DTDS algorithm performs the best at MAO, with the highest R and the smallest error values,
281   surpassing even those of the SGP site, where the DTDS algorithm was developed and tested.
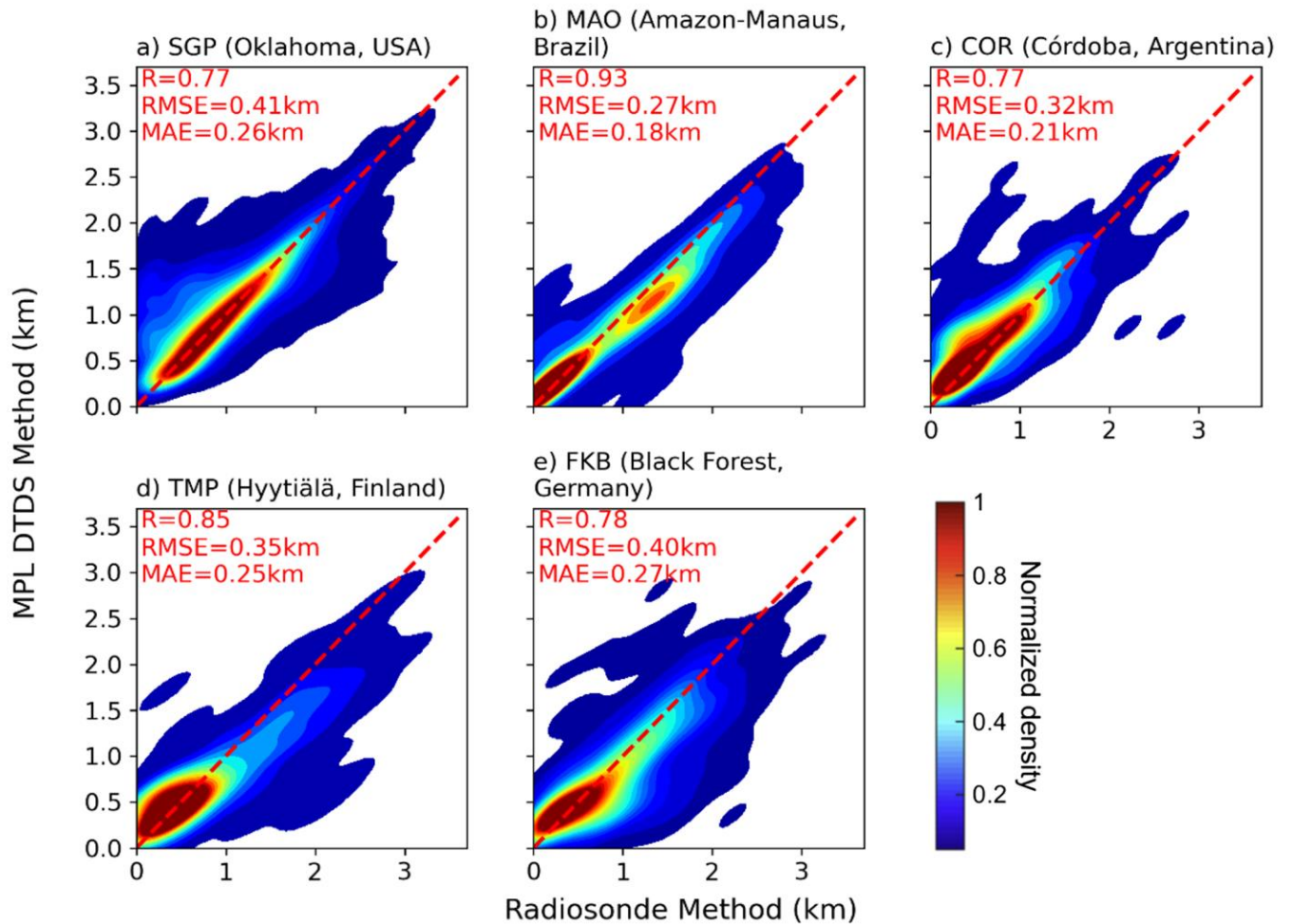

282

Figure 5. Kernel distribution estimates for the MPL-based DTDS PBLH and the radiosonde PBLH based on the Liu–Liang method using virtual potential temperatures at the five ARM sites. The correlation coefficient (R), root-mean-square error (RMSE), and mean absolute error (MAE) are given in each panel. Dashed red lines correspond to 1:1 lines.
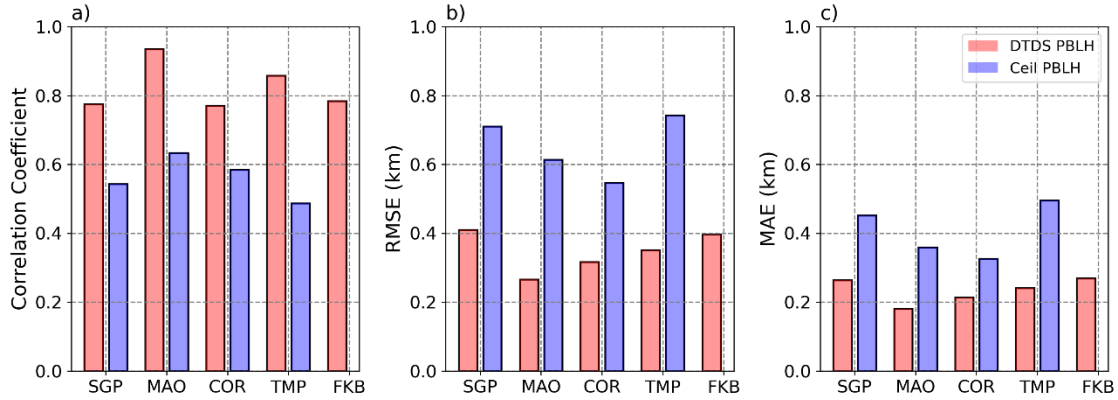

Figure 6. Correlation coefficients, RMSEs, and MAEs from the DTDS- and radiosonde-derived PBLH relations (red bars) and the ceilometer- and radiosonde-derived PBLH relations (blue bars) at the five ARM sites.

The overestimation of shallow boundary layers generally occurs during the morning hours when the PBL tends to be stable and highly stratified. Both conditions pose difficulties in estimating the PBLH based on backscatter information, which is more related to lidar limitations than to problems in the DTDS algorithm. For example, in the case of extratropical sites like SGP, the performance of the DTDS algorithm varies with season. Retrievals from the SGP site have higher errors during winter because the PBLH tends to be shallower than in other seasons. The PBLH can sometimes be below the near-surface 150-m MPL blind zone of the region, impeding the correct estimation of the PBLH.

3.3 Analysis of errors and limitations

The analysis of errors and limitations in the performance of the DTDS algorithm reveals that attributing all inaccuracies solely to the algorithm itself would be overly simplistic. Instead, this subsection comprehensively examines the multiple sources of errors, including those resulting from lidar measurements and limitations, radiosondes measurements, and the RS-PBLH algorithm. By delving into these factors, light will be shed on the intricate interplay between these components, highlighting the inherent complexity of the PBLH retrieval. At the same time, this error analysis will help recognize areas for potential enhancement and underscore the need for further refinement of the DTDS algorithm.

a) Errors in the radiosonde estimation

A source of errors that needs special attention is errors associated with the RS-PBLH algorithm. RS-PBLH retrievals are widely accepted in the scientific community as the ground truth.

312 However, even though radiosonde measurements are the most reliable source to estimate the
313 PBLH, the computed PBLH can sometimes be ambiguous. Radiosonde-based thermodynamic
314 profiles can be vague, e.g., when there are multiple inversion layers or no inversions. Both
315 situations complicate the PBLH retrieval, leading to great uncertainty. Furthermore, algorithms
316 that use radiosonde information to compute the PBLH are also susceptible to errors, given the
317 multiple parameters needed that are not necessarily adjusted to local environmental conditions,
318 such as the multiple threshold values needed in the Liu and Liang method. The computed PBLH
319 based on radiosonde measurements can also vary depending on the chosen thermodynamic
320 variable, namely the Potential Temperature ($\boldsymbol{\theta}$) or the Virtual Potential Temperature ($\boldsymbol{\theta_v}$) (Liu &
321 Liang, 2010).

322 Figure 7b illustrates the PBLH computed at MAO on 14 September 2015, along with the
323 backscatter information during a relatively clear-sky day with a highly stratified aerosol profile.
324 Note the elevated aerosol layer signal during the early morning that progressively disappears as
325 the day evolves. At noon, the DTDS-PBLH algorithm retrieves the PBLH around 1.5 km,
326 corresponding to the approximate location of the aerosol layer. The RS-PBLH algorithm
327 identifies the PBLH at ~2.5 km. To better understand this discrepancy, Fig. 7a presents $\boldsymbol{\theta}$ and $\boldsymbol{\theta_v}$
328 profiles measured near noon. Also shown is the height of the PBLH identified by the RS-PBLH
329 algorithm. In both temperature profiles, there is one capping inversion near 1.5 km and a weaker
330 one around 2.5 km, where the Liu and Liang algorithm estimates the PBLH. Multiple inversion
331 layers in a temperature profile pose a challenge when attempting to identify the PBLH based
332 solely on thermodynamic considerations because deciding which of the inversion layers should
333 be considered as the PBLH can be ambiguous. In this case, lidar data provides extra information
334 to better describe the PBL. Here, the capping inversion around 1.5 km aligns with the DTDS-
335 PBLH estimate and the extension of the aerosol layer, suggesting that this position would be
336 more appropriate as the PBLH instead of the second inversion around 2.5 km, which the RS-
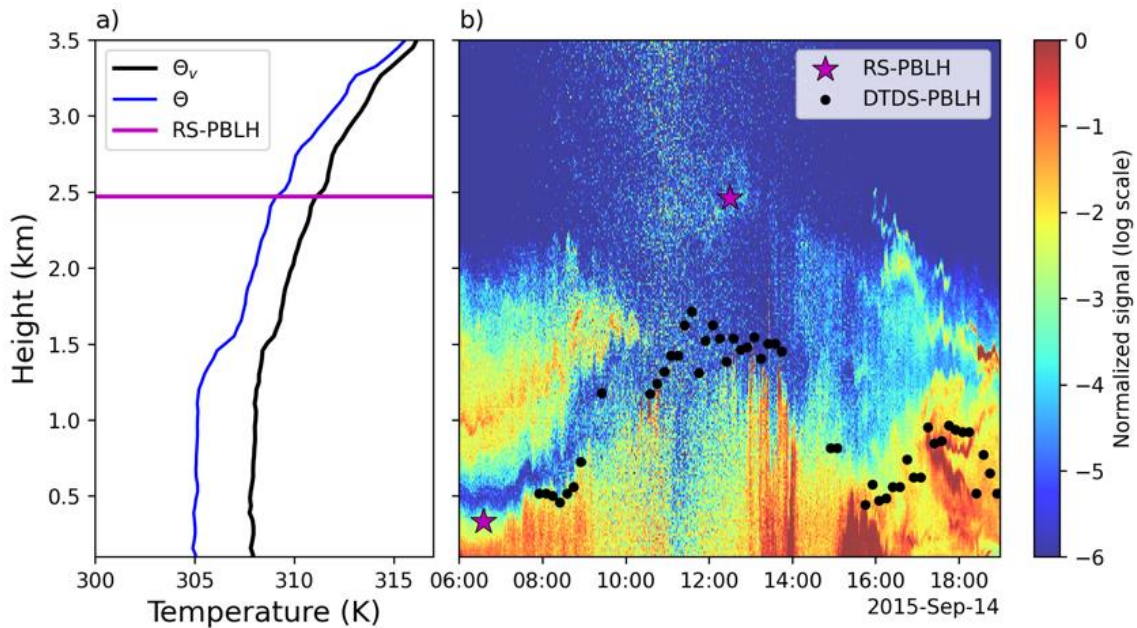337 PBLH algorithm assigns as the PBLH.

338

Figure 7. PBLHs at MAO on 14 September 2015. (a) Profiles of potential temperature (θ) and virtual potential temperature (θ_v) measured around noon on the same date (black and blue lines, respectively). The magenta line corresponds to the RS-PBLH. In this example, RS-PBLHs based on θ and θ_v, and the ARM RS-PBLH have the same values. Therefore, only one line is shown. (b) Backscatter information for the same day where the colormap indicates the normalized backscatter signal. Black dots correspond to DTDS-PBLHs, while stars are RS-PBLHs.

As mentioned previously, differences between the RS-PBLH and the DTDS-PBLH retrievals also depend on the type of temperature used to compute the PBLH. Figure 8 is like Figure 5 but uses θ_v instead of θ to compute the RS-PBLH. While these figures are similar, they are not identical. Overall, the PBLH computed using θ performs better than the one using θ_v because θ_v contains considerable uncertainties due to errors measuring humidity (Liu & Liang, 2010). However, for three of the five sites, the correlation coefficient between RS-PBLH and DTDS-PBLH retrievals is higher, going from 0.77 to 0.79 at SGP, from 0.85 to 0.87 at TMP, and from 0.78 to 0.81 at FKB, albeit with a slightly higher RMSE of ~0.1 km. The higher correlation observed at these three sites implies that the dispersion observed in the KDE functions is influenced not only by the performance of the DTDS algorithm but also by the various complexities inherent in the RS-PBLH. This finding suggests that there is room for improvement in the accuracy of RS-PBLH estimates as well.
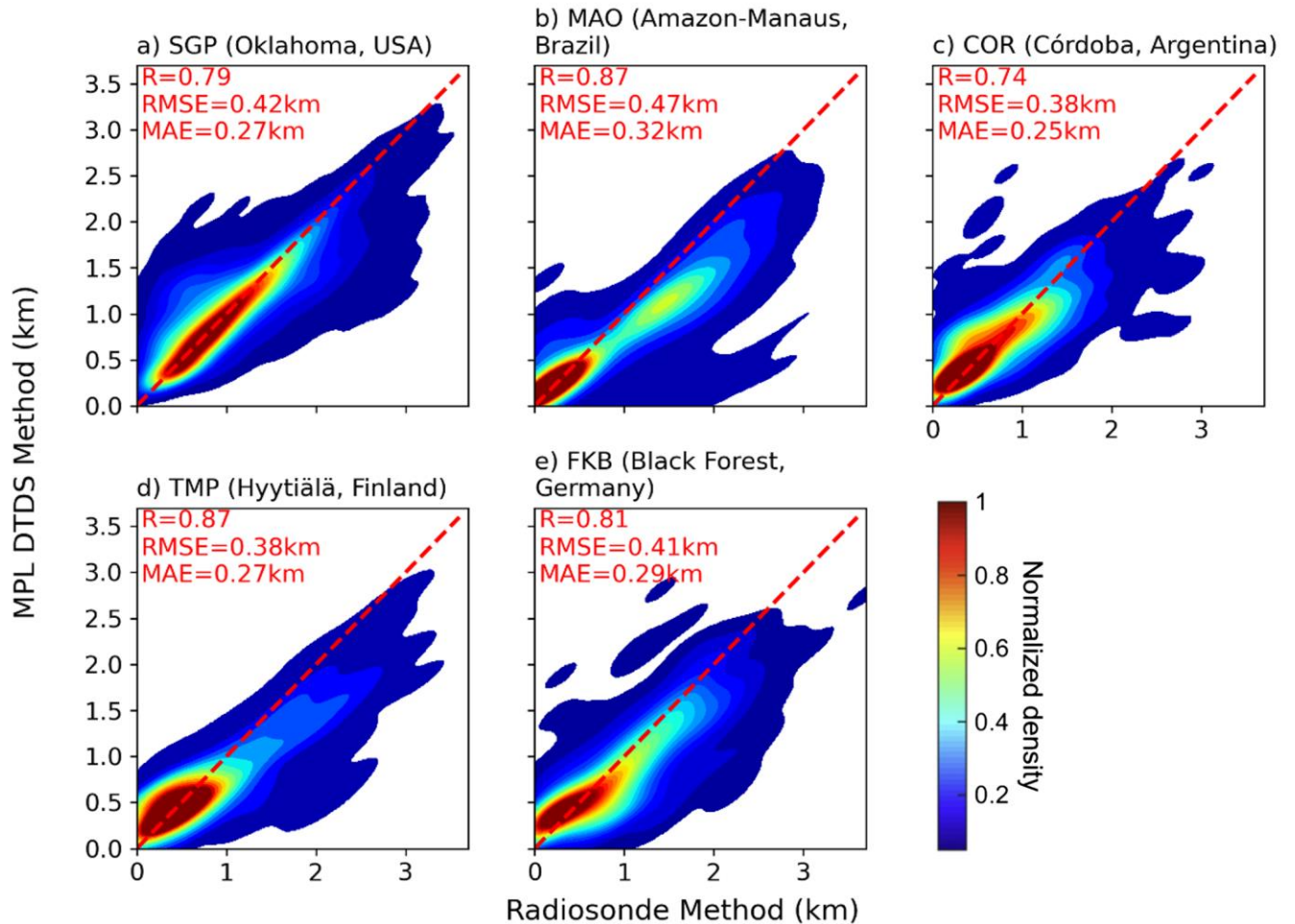

Figure 8. Same as Fig. 5, but instead of using θ to compute the PBLH, θ_v was used.

359   The distinction between RS-PBLH calculated using $\boldsymbol{\theta}$ and $\boldsymbol{\theta_v}$ is demonstrated in Fig. 9, showing
360   KDEs between RS-PBLH based on $\boldsymbol{\theta}$ and $\boldsymbol{\theta_v}$ at the five ARM sites. Among these sites, the two
361   sets of RS-PBLH estimates agree the best at FKB, with an R of 0.95 and an RMSE of 0.2 km.
362   The worse agreement is seen at MAO, with an R of 0.92 and an RMSE of 0.33 km. At all sites
363   except FKB, the RS-PBLH based on $\boldsymbol{\theta_v}$ consistently yields higher values than the RS-PBLH
364   based on θ, contributing significantly to the larger RMSE observed, particularly at locations like
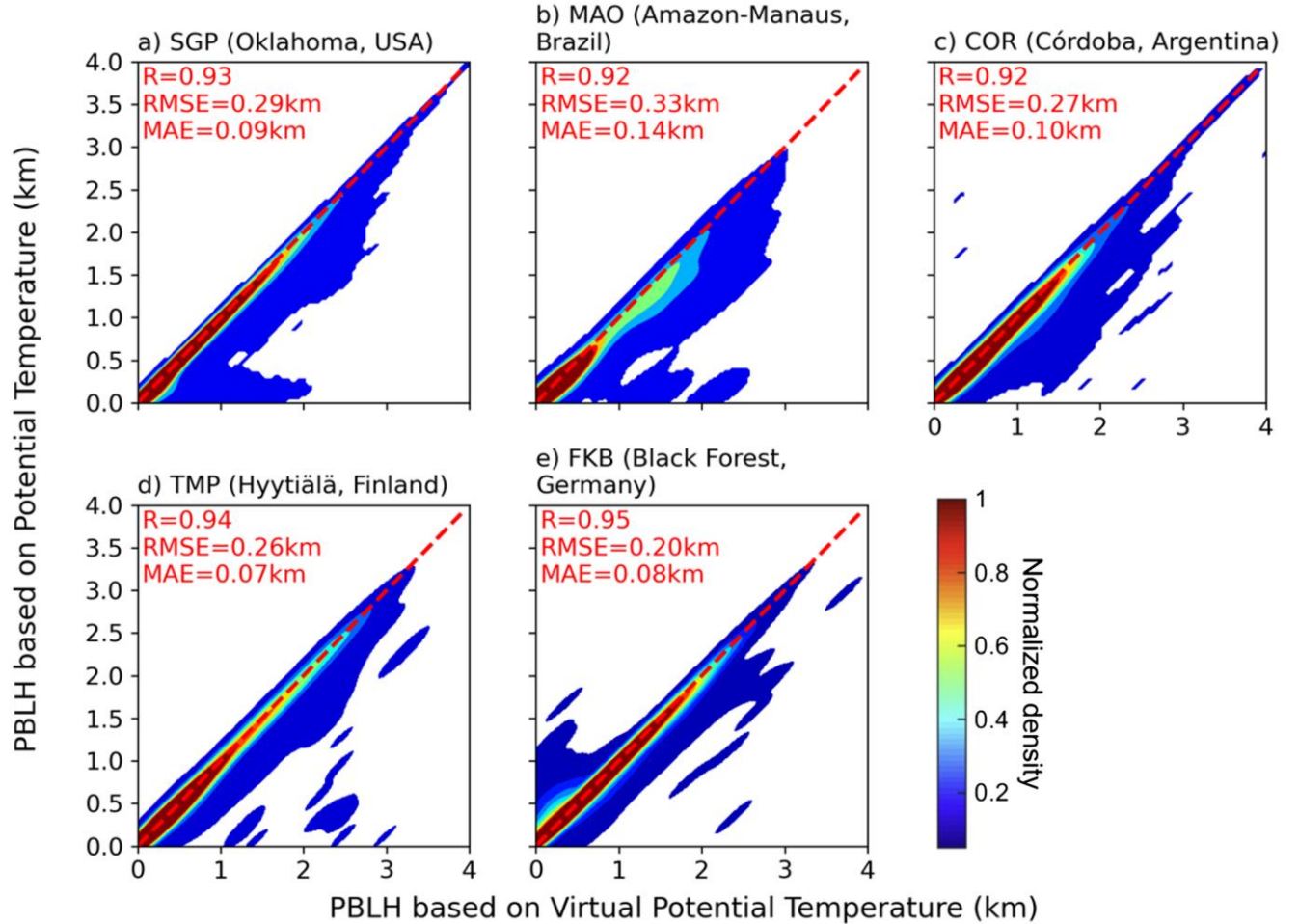365   MAO.

366
367 **Figure 9.** Kernel distribution estimates for radiosonde PBLHs based on potential temperature
368 and virtual potential temperature at the five ARM sites. The correlation coefficient (R), root-
369 mean-square error (RMSE), and mean absolute error (MAE) are given in each panel. Dashed red
370 lines correspond to 1:1 lines.

371   **b) Errors and limitations of the MPL**

372   Another important source of errors arising when computing the DTDS-PBLH is that resulting
373   from lidar limitations. For example, Fig. 10 showcases a situation that occurred over TMP on 15
374   February 2014. On that day, the presence of a stratocumulus-topped boundary layer (STBL)
375   attenuated the MPL backscatter, preventing the instrument from sensing the atmosphere beyond
376   the cloud-base height. In this case, the DTDS algorithm retrieves the PBLH at the same height as
377   the cloud base at ~0.7 km. However, when looking at the temperature profiles around noon in

378   Fig. 10a, a well-mixed boundary layer with a strong capping inversion at ~1.1 km is seen. This
379   inversion aligns with the cloud-top height shown in Fig. 10a. Considering that the PBLH is
380   defined as the maximum altitude influenced by the earth's surface, the RS-PBLH would be a
381   better estimate of the PBLH. The presence of an STBL and the limited capability of the MPL
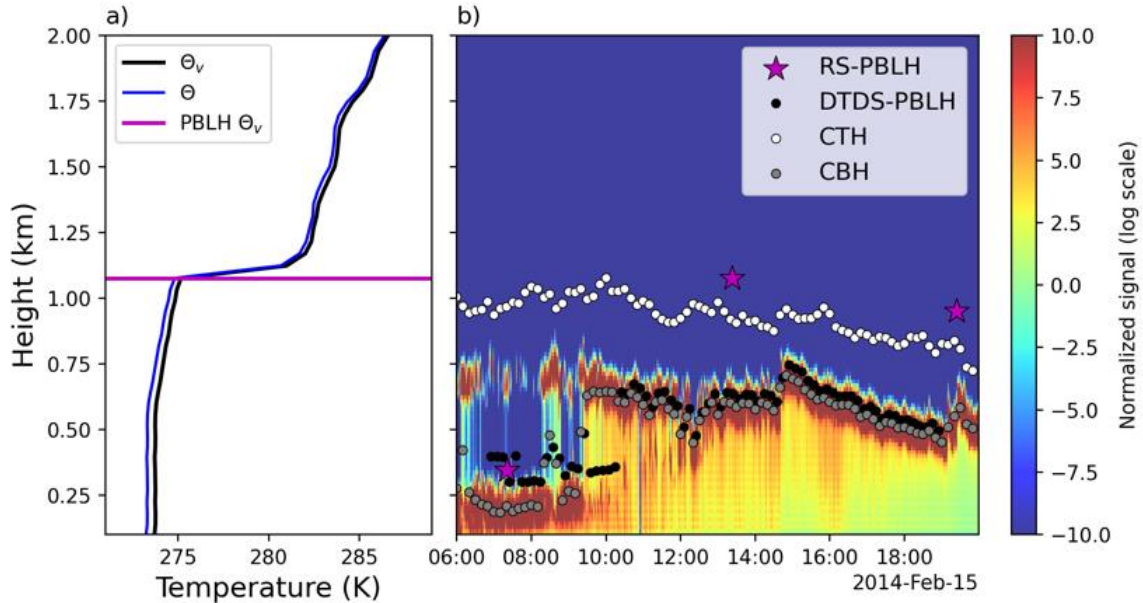382   under cloudy conditions introduces errors in such cases.

383
384   **Figure 10.** PBLHs at TMP on 22 October 2014. (a) Profiles of potential temperature (θ) and
385   virtual potential temperature (θ_v) measured around noon on the same date (black and blue lines,
386   respectively). The magenta line corresponds to the RS-PBLH. For this example, RS-PBLH based
387   on θ and θ_v, and the ARM RS-PBLH have the same values. Therefore, only one line is shown.
388   (b) Backscatter information for the same day where the colormap indicates the normalized
389   backscatter signal. Black dots correspond to DTDS-PBLHs, stars are RS-PBLHs, white dots are
390   cloud-top heights (CTH), and grey dots are cloud-base heights (CBH).

391   The performance of the DTDS algorithm is notably diminished in instances where the lidar
392   instrument is not operating properly. The COR site provides an example of the errors that arise
393   from poor lidar performance. The initial MPL installed at the COR site was misaligned, leading
394   to a consistent spurious signal always present in the backscatter profile. Figure 11 shows two
395   different days when the MPL at COR was misaligned, one under clear-sky conditions and a
396   second under cloudy conditions. In both cases, a strong constant step signal is visible between
397   0.5 and 1 km. This spurious signal in the backscatter profile impeded the accurate determination
398   of the PBLH on the clear-sky day, resulting in the DTDS algorithm incorrectly placing the PBLH
399   at ~0.8 km. In the case when boundary-layer clouds were present (Fig. 11b), the strong
400   backscatter signal from the clouds counteracted the spurious backscatter signal, helping the
401   DTDS algorithm accurately retrieve the PBLH and resulting in a better agreement between the
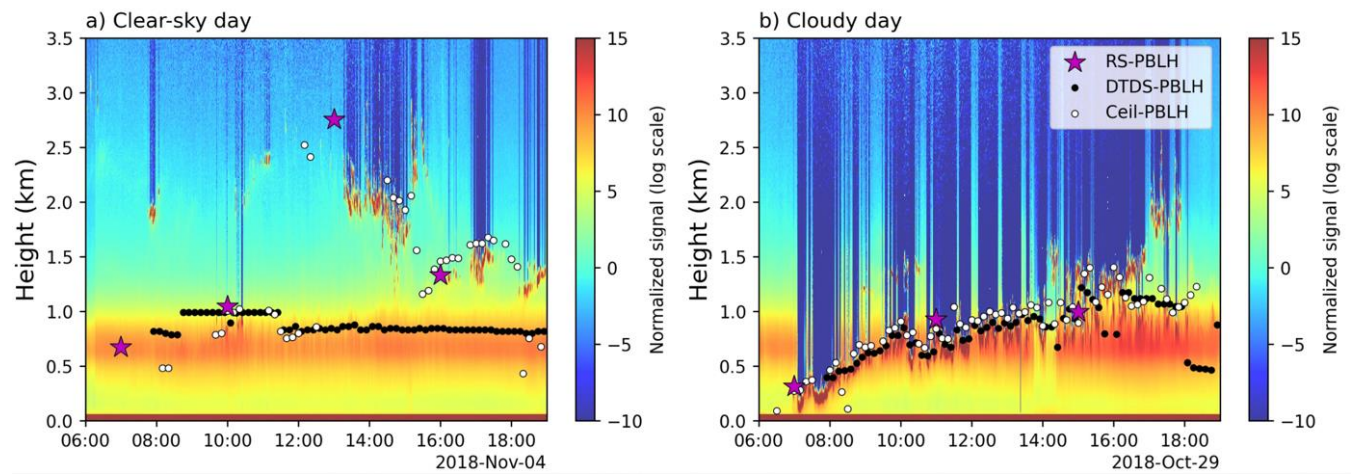402   DTDS-PBLH, Ceil-PBLH, and RS-PBLH retrievals.

Figure 11. PBLHs at COR using the DTDS algorithm (black dots), the ARM Ceil-PBLH
product (white dots), and radiosonde estimates (magenta stars) prior to the replacement of the
MPL on (a) a clear-sky day and (b) a cloudy day. The colormap indicates the normalized
backscatter signal measured by the MPL. The constant orange-red belt observed between 0.5 and
1 km represents spurious signals.

409 To address the misalignment issue in the MPL, a new lidar was installed at the site on 18
410 February 2019. This replacement successfully eliminated the spurious signal, leading to a notable
411 improvement in the performance of the DTDS algorithm. Figure 12 compares the DTDS
412 performance at retrieving the PBLH before and after the MPL was changed under clear-sky and
413 cloudy conditions. Note that erroneous DTDS-PBLH estimates were included because the
414 primary aim is to highlight the pronounced improvements observed in the DTDS performance
415 exclusively resulting from replacing the lidar. Overall, R is higher (Fig. 12a), and the RMSE is
416 smaller (Fig. 12b) under cloudy conditions than under clear-sky conditions. Also, after the MPL
417 was replaced, R increased from 0.58 to 0.7 on average, and RMSE decreased from 0.48 km to
418 0.37 km. In the case of the MAEs, we also see a slight improvement when the lidar is changed,
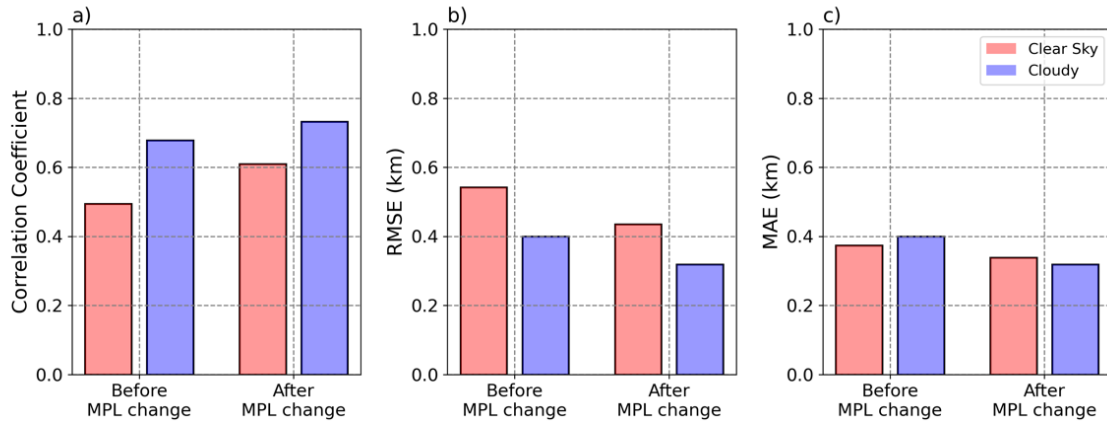419 even considering that the MAE weighs all errors equally.

420

421 **Figure 12.** (a) Correlation coefficients, (b) RMSEs, and (c) MAEs from the DTDS- and
422 radiosonde-derived PBLH relations before and after the MPL was replaced at the COR site. Red
423 bars correspond to clear-sky conditions, and blue bars represent cloudy conditions.

424 **5 Conclusions**

425 Gaining a comprehensive understanding of the planetary boundary layer height (PBLH) is
426 crucial for advancing our knowledge across numerous atmospheric processes and applicable
427 fields. Despite the longstanding reliance on radiosondes for PBLH measurements, there is a
428 pressing need to enhance the precision of PBLH estimates, particularly when applying lidar
429 techniques. Over recent years, lidar systems have been increasingly used to estimate the PBLH,
430 primarily because they overcome a key limitation of traditional radiosonde estimates, namely,
431 the lack of temporal resolution. Lidar methods allow for continuous PBLH monitoring, thereby
432 advancing our grasp of atmosphere-surface processes and the evolution of the PBL. However,
433 lidar systems have their own inherent limitations to incur considerable uncertainties and biases,
434 especially under stable and highly stratified conditions.

435 The DOE ARM project has deployed an extensive network of MPL systems in many places,
436 thereby presenting a valuable opportunity to investigate PBLH in different parts of the world. In
437 this study, we took advantage of this large network by evaluating the performance of the
438 Different Thermo-Dynamic Stabilities (DTDS) algorithm developed by our team (Su et al.,
439 2020). It was aimed to tackle with a common problem of incoherent variations between
440 atmospheric thermodynamics and the backscattering of aerosols chiefly in early morning by

441 modifying the traditional wavelet method for enhancing temporal and spatial coherence. The
442 DTDS algorithm was developed and tested for calculating PBLHs at the SGP site, the ARM's
443 primary permanent sites where it shows superior performance over the conventional wavelet and
444 gradient methods attested by higher correlations and smaller RMSE but its performance at other
445 places of different conditions are unknown.

446 The DTDS is thus evaluated at five ARM observatories situated in different continents (North
447 America, South America, and Europe) where more than six months of MPL data were available.
448 Notably, the DTDS-PBLH and the radiosonde-derived PBLH agreed well, with R ranging from
449 0.77 at the COR site to 0.93 at the MAO site, and the root-mean-square error ranging 0.27 km at
450 MAO to 0.41 km at SGP. The correlation and the RMSE instill confidence in the new method's
451 robustness in representing the boundary layer's temporal variability, thus unveiling new
452 possibilities for studying surface atmospheric processes. Compared to existing PBLH products
453 for the same sites, e.g., Ceil-PBLH, the RMSEs of DTDS-PBLH were roughly a third smaller
454 than the RMSE of Ceil-PBLH. On the other hand, the MAEs of DTDS-PBLH were half smaller
455 than the MAEs of Ceil-PBL. Current lidar-based RMSE of PBLH estimates at the five different
456 sites were close to 0.6 km, which is reduced to less than 0.4 km for the DTDS-derived PBLH. In
457 the case of the MAE, the current ceil-PBLH errors were close to 0.41 km that is reduced to an
458 average of 0.23 km for the DTDS.

459 Despite the relatively superior performance, both the DTDS algorithm and input data suffer from
460 limitations, leading to retrieval errors in the PBL product. Besides, there also exist uncertainties
461 in radiosonde-based PBLH estimates due to the complexity of atmospheric thermodynamics. For
462 example, at the COR site, lidar misalignments in the first MPL installed there produced a
463 spurious signal that hampered the DTDS performance. Further limitations in the DTDS
464 algorithm include constraints in the MPL visibility, such as during cloudy conditions that
465 attenuate the backscatter signal. Radiosonde measurements may also introduce ambiguity in
466 determining the PBLH, causing disparities between radiosonde and DTDS estimates, especially
467 when multiple inversion layers are present or when there are no inversions. Moreover, the
468 thermodynamic variable used in calculating the radiosonde-derived PBLH (e.g., potential
469 temperature or virtual potential temperature) can introduce variability in the results. A thorough
470 understanding of these errors and limitations is pivotal for continuous improvements in the
471 DTDS algorithm, enhancing its performance and reliability in estimating PBLH.

472 **Acknowledgments**

477 **Data availability**

478 All ARM data at five sites are publicly available at the USA Department of Energy Atmospheric
479 Radiation Measurement Data Center: https://www.arm.gov/capabilities/instruments/sonde. The
480 planetary boundary layer height derived from DTDS over the Southern Great Plains can be
481 downloaded from https://doi.org/10.5281/zenodo.7374849.
482

483 **References**

484 Bradley, R. S., Keimig, F. T., and Diaz, H. F.: Recent changes in the north American arctic

485 boundary layer in winter, J. Geophys. Res-Atmos., 98, 8851–8858,

486 https//doi:10.1029/93JD00311, 1993.

487 Brooks, I. M.: Finding boundary layer top: application of a wavelet covariance transform to lidar

488 backscatter profiles, J. Atmos. Ocean. Tech., 20(8), 1092–1105, https://doi:10.1175/1520-

489 0426(2003)020<1092:FBLTAO>2.0.CO;2, 2003.

490 Campbell, J. R., Hlavka, D. L., Welton, E. J., Flynn, C. J., Turner, D. D., Spinhirne, J. D., Scott,

491 V. S., and Hwang, I. H.: Full-time, eye-safe cloud and aerosol lidar observation at atmospheric

492 radiation measurement program sites: instruments and data processing, J. Atmos. Ocean. Tech.,

493 19(4), 431–442, https://doi:10.1175/1520-0426(2002)019<0431:FTESCA>2.0.CO;2, 2002.

494 Campbell, J. R., Welton, E. J., Spinhirne, J. D., Ji, Q., Tsay, S.-C., Piketh, S. J., Barenbrug, M.,

495 and Holben, B. N.: Micropulse lidar observations of tropospheric aerosols over northeastern

496 South Africa during the ARREX and SAFARI 2000 dry season experiments, J. Geophys. Res-

497 Atmos., 108(D13), https://doi:10.1029/2002JD002563, 2003.

498 Eresmaa, N., Karppinen, A., Joffre, S. M., Räsänen, J., and Talvitie, H.: Mixing height

499 determination by ceilometer, Atmos. Chem. Phys., 6(6), 1485–1493, https://doi:10.5194/ACP-6-

500 1485-2006, 2006.

501 Guo, J., Miao, Y., Zhang, Y., Liu, H., Li, Z., Zhang, W., He, J., Lou, M., Yan, Y., Bian, L., and

502 Zhai, P.: The climatology of planetary boundary layer height in China derived from radiosonde

503 and reanalysis data, Atmos. Chem. Phys., 16(20), 13,309–13,319, https://doi:10.5194/acp-16-

504 13309-2016, 2016.

505   Holdridge, D.: Balloon-borne sounding system (SONDE) instrument handbook,

506   https://www.arm.gov/publications/tech_reports/handbooks/sonde_handbook.pdf, 2020.

507   Hu, X. M., Nielsen-Gammon, J. W., and Zhang, F.: Evaluation of three planetary boundary layer

508   schemes in the WRF model, J. Appl. Meteorol. Clim., 49(9), 1831–1844,

509   https://doi:10.1175/2010JAMC2432.1, 2010.

510   Knote, C., Tuccella, P., Curci, G., Emmons, L., Orlando, J. J., Madronich, S., Baró, R., Jiménez-

511   Guerrero, P., Luecken, D., Hogrefe, C., Forkel, R., Werhahn, J., Hirtl, M., Pérez, J. L., San José,

512   R., Giordano, L., Brunner, D., Yahya, K., and Zhang, Y.: Influence of the choice of gas-phase

513   mechanism on predictions of key gaseous pollutants during the AQMEII phase-2

514   intercomparison, Atmos. Environ., 115, 553–568,

515   https://doi:10.1016/J.ATMOSENV.2014.11.066, 2015.

516   Li, H., Liu, B., Ma, X., Jin, S., Ma, Y., Zhao, Y., and Gong, W.: Evaluation of retrieval methods

517   for planetary boundary layer height based on radiosonde data, Atmos. Meas. Tech., 14(9), 5977–

518   5986, https://doi:10.5194/amt-14-5977-2021, 2021.

519   Li, Z., Guo, J., Ding, A., Liao, H., Liu, J., Sun, Y., Wang, T., Xue, H., Zhang, H. and Zhu, B.:

520   Aerosol and boundary-layer interactions and impact on air quality. National Science Review,

521   4(6), pp.810-833, 2017.

522   Liu, S., and Liang, X. Z.: Observed diurnal cycle climatology of planetary boundary layer height,

523   J. Climate, 23(21), 5790–5809, https://doi:10.1175/2010JCLI3552.1, 2010.

524   Liu, B., Ma, Y., Gong, W., Jian, Y., and Ming, Z.: Two-wavelength lidar inversion algorithm for

525   determining planetary boundary layer height, J. Quant. Spectrosc. Ra., 206, 117–124,

526   https://doi:10.1016/J.JQSRT.2017.11.008, 2018.

527   Munkel, C., and Rasanen, J.: New optical concept for commercial lidar ceilometers scanning the

528   boundary layer, P. Soc. Photo-Opt. Ins., 5571, 364-374, 2004.

529   Münkel, C., Eresmaa, N., Räsänen, J., and Karppinen, A.: Retrieval of mixing height and dust

530   concentration with lidar ceilometer, Bound-Lay. Meteorol., 124, 117-128, 2007.

531   Sawyer, V., and Li, Z.: Detection, variations and intercomparison of the planetary boundary

532   layer depth from radiosonde, lidar and infrared spectrometer, Atmos. Environ., 79, 518–528,

533   https://doi:10.1016/j.atmosenv.2013.07.019, 2013.

534   Seibert, P.: Review and intercomparison of operational methods for the determination of the

535   mixing height, Atmos. Environ., 34(7), 1001–1027, https://doi:10.1016/S1352-2310(99)00349-0,

536   2000.

537   Seidel, D. J., Ao, C. O., and Li, K.: Estimating climatological planetary boundary layer heights

538   from radiosonde observations: comparison of methods and uncertainty analysis, J. Geophys. Res-

539   Atmos., 115(D16), 16113, https://doi:10.1029/2009JD013680, 2010.

540   Stull, R. B.: An introduction to boundary layer meteorology, 13, Springer Science & Business

541   Media, 1988.

542   Romps, D. M.: Exact expression for the lifting condensation level, J. Atmos. Sci., 74, 3891–

543   3900, https://doi.org/10.1175/JAS-D-17-0102.1, 2017.

544   Su, T., Li, Z. and Zheng, Y.: Cloud-Surface Coupling Alters the Morning Transition From Stable

545   to Unstable Boundary Layer. Geophysical Research Letters, 50(5), p.e2022GL102256, 2023.

546   Su, T., Li, Z., and Kahn, R.: A new method to retrieve the diurnal variability of planetary

547   boundary layer height from lidar under different thermodynamic stability conditions, Remote

548   Sens. Environ., 237, 111519, https://doi:10.1016/j.rse.2019.111519, 2020.

549   Su, T., Zheng, Y., and Li, Z.: Methodology to determine the coupling of continental clouds with

550   surface and boundary layer height under cloudy conditions from lidar and meteorological

551   data, Atmos. Chem. Phys., 22(2), 1453-1466, https://doi.org/10.5194/acp-22-1453-2022, 2022.

552   Vogelezang, D. H. P., and Holtslag, A. A. M.: Evaluation and model impacts of alternative

553   boundary-layer height formulations, Bound-Lay Meteorol, 81, 245–269.

554   https://doi:10.1007/BF02430331, 1996.

555   Zhang, D., Comstock, J., and Morris, V.: Comparison of planetary boundary layer height from

556   ceilometer with ARM radiosonde data, Atmos. Meas. Tech., 15(16), 4735–4749,

557   https://doi:10.5194/amt-15-4735-2022, 2022.

558   Zhang, W., Guo, J., Miao, Y., Liu, H., Song, Y., Fang, Z., He, J., Lou, M., Yan, Y., Li, Y., and

559   Zhai, P.: On the summertime planetary boundary layer with different thermodynamic stability in

560   China: A Radiosonde Perspective, J. Climate, 31(4), 1451–1465, https://doi:10.1175/JCLI-D-17-

561   0231.1, 2018.

562   Zhang, W., Guo, J., Miao, Y., Liu, H., Zhang, Y., Li, Z., and Zhai, P.: Planetary boundary layer

563   height from CALIOP compared to radiosonde over China, Atmos. Chem. Phys., 16(15), 9951–

564   9963, https://doi:10.5194/acp-16-9951-2016, 2016.

565